3-17-1997

Application of a Finite-Volume Time-Domain Technique to Three-Dimensional Objects

Frederick G. Harmon
Cedarville University, fharmon@cedarville.edu

A. J. Terzuoli

APPLICATION OF A FINITE-VOLUME TIME-DOMAIN TECHNIQUE TO THREE-DIMENSIONAL OBJECTS

Frederick G. Harmon, Andrew J. Terzuoli, Jr.
Air Force Institute of Technology

Abstract-Concurrent engineering approaches for the disciplines of computational fluid dynamics (CFD) and electromagnetics (CEM) are necessary for designing future high-performance aircraft. A characteristic-based finite-volume time-domain (FVTD) computational algorithm used by CFD and herein applied to CEM is implemented to analyze the radar cross section (RCS) of two three-dimensional objects, the ogive and cone-sphere, by utilizing a scattered-field formulation of the time-dependent Maxwell equations. The FVTD formulation uses a monotone upstream-centered scheme for conservation laws (MUSCL) for the flux evaluation and a Runge-Kutta multi-stage scheme for the time integration. The RCS results are obtained from the electromagnetic fields via a Fourier transform and a near-to-far field transformation.

The FVTD code and algorithm are evaluated for electromagnetic scattering problems by comparing FVTD code RCS results to data obtained from a Moment Method (MoM) code (CICERO) and empirical RCS data published by the Electromagnetic Code Consortium (EMCC). The FVTD RCS results for the ogive and cone-sphere are within 3.0 dB of the bistatic MoM results and 3.1 dB of the monostatic empirical RCS data. Accurate FVTD computations of diffraction, traveling waves, and creeping waves require a surface grid point density of 15-30 cells/λ, dependent on frequency.

I. FVTD Formulation of Maxwell Equations

The FVTD computational technique is capable of concurrently solving the Euler equations of fluid dynamics and the Maxwell equations of electromagnetics. CFD has used the FVTD technique since the early 1980's [21] to analyze the airflow about an aircraft or airfoil and the technique has recently been applied to CEM. Several engineers, Blake, Shang, Shankar [2-3, 7-20] and others are exploring and advancing the application of the FVTD technique to the Maxwell equations of electromagnetics. The FVTD formulation and numerical procedure implemented in Shang's FVTD code is discussed and used to obtain the RCS results for the ogive and cone-sphere.

A. Grid Generation of Finite-Volume Cells

To use FVTD, the physical space surrounding an object of interest must be discretized into volumetric cells. The space containing the finite-volume cells is referred to as the space grid [22]. The frequency of interest and the electrical length of the object determines the number of cells in the grid.

For the characteristic-based FVTD formulation, a structured grid using curvilinear coordinates is used so the wave propagation is aligned closely with one of the coordinate axes [10]. The compatibility condition used for the radiation boundary condition is exact if the wave propagation parallels a coordinate axis. In addition, the curvilinear coordinates permit higher accuracy in the computation of the electric and magnetic scattered fields.

B. Maxwell's Equations in Conservation Form

The two time-domain Maxwell curl equations, in differential form, are shown below and will be used in the development of the electromagnetic FVTD equations:

Faraday's Law: $$\nabla \times \boldsymbol{E} = -\frac{\partial \boldsymbol{B}}{\partial t} \qquad (1)$$

Ampere's Law: $$\nabla \times \boldsymbol{H} = \frac{\partial \boldsymbol{D}}{\partial t} + \boldsymbol{J} \qquad (2)$$

where $\boldsymbol{E}$: Electric field strength vector (V/m)
$\boldsymbol{B}$: Magnetic flux density vector (Wb/m^2 or T)
$\boldsymbol{D}$: Electric flux density vector (C/m^2)
$\boldsymbol{J}$: Electric current density vector (A/m^2)
$\boldsymbol{H}$: Magnetic field strength vector (A/m)

Using the constitutive parameters to relate the field strength vectors and the flux density vectors, when the material is linear and isotropic, the constitutive relations are $D = \varepsilon E$ and $B = \mu H$ where ε is the electric permittivity (F/m) and μ is the magnetic permeability (H/m).

For use in FVTD, the two Maxwell equations are cast in conservation form [12]. The solution of Maxwell's equations do not require the conservation form; however, the form is required by the Euler equations to conserve physical properties such as energy, mass, and momentum. The Maxwell equations are cast in conservation form solely to take advantage of the

same computational technique used to solve the Euler equations. To this end, the curl operations are carried out and the constitutive parameters are implemented. The result is given by

$$\frac{\partial \boldsymbol{U}}{\partial t}+\frac{\partial \boldsymbol{F}}{\partial x}+\frac{\partial \boldsymbol{G}}{\partial y}+\frac{\partial \boldsymbol{H}}{\partial z}=-\boldsymbol{J} \tag{3}$$

where

$$\boldsymbol{U}=\begin{bmatrix} B_x \\ B_y \\ B_z \\ D_x \\ D_y \\ D_z \end{bmatrix} \quad \boldsymbol{F}=\begin{bmatrix} 0 \\ -D_z/\varepsilon \\ D_y/\varepsilon \\ 0 \\ B_z/\mu \\ -B_y/\mu \end{bmatrix} \quad \boldsymbol{G}=\begin{bmatrix} D_z/\varepsilon \\ 0 \\ -D_x/\varepsilon \\ -B_z/\mu \\ 0 \\ B_x/\mu \end{bmatrix} \quad \boldsymbol{H}=\begin{bmatrix} -D_y/\varepsilon \\ D_x/\varepsilon \\ 0 \\ B_y/\mu \\ -B_x/\mu \\ 0 \end{bmatrix} \quad \boldsymbol{J}=\begin{bmatrix} 0 \\ 0 \\ 0 \\ J_x \\ J_y \\ J_z \end{bmatrix}$$

Equation (3) is a system of six linear equations. $\boldsymbol{U}$ is the independent variable and the $\boldsymbol{F}$, $\boldsymbol{G}$, and $\boldsymbol{H}$ flux vectors are the dependent variables. The equations are not linearly independent; therefore, a characteristic-based technique is used to uncouple the six equations.

C. Coordinate Transformation

To analyze the scattering of various objects, such as the ogive and cone-sphere, a curvilinear coordinate transformation is required. A curvilinear structured grid minimizes the errors introduced in the cell metrics and the flux calculations. The variables ξ, η, and ζ are used to convert the Cartesian coordinates to curvilinear coordinates. After a coordinate transformation, Equation (3) becomes [12, 13]

$$\frac{\partial \hat{\boldsymbol{U}}}{\partial t}+\frac{\partial \hat{\boldsymbol{F}}}{\partial \xi}+\frac{\partial \hat{\boldsymbol{G}}}{\partial \eta}+\frac{\partial \hat{\boldsymbol{H}}}{\partial \zeta}=-\hat{\boldsymbol{J}} \tag{4}$$

where $\hat{\boldsymbol{U}}=\dfrac{\boldsymbol{U}}{V} \qquad \hat{\boldsymbol{J}}=\dfrac{\boldsymbol{J}}{V}$

$$\hat{\boldsymbol{F}}=\left(\frac{\partial \xi}{\partial x}\boldsymbol{F}+\frac{\partial \xi}{\partial y}\boldsymbol{G}+\frac{\partial \xi}{\partial z}\boldsymbol{H}\right)\frac{1}{V} \qquad \hat{\boldsymbol{G}}=\left(\frac{\partial \eta}{\partial x}\boldsymbol{F}+\frac{\partial \eta}{\partial y}\boldsymbol{G}+\frac{\partial \eta}{\partial z}\boldsymbol{H}\right)\frac{1}{V} \qquad \hat{\boldsymbol{H}}=\left(\frac{\partial \zeta}{\partial x}\boldsymbol{F}+\frac{\partial \zeta}{\partial y}\boldsymbol{G}+\frac{\partial \zeta}{\partial z}\boldsymbol{H}\right)\frac{1}{V}$$

and V is the Jacobian of the coordinate transformation.

D. Finite-Volume Formulation

Equation (4) is applied to every finite-volume cell in the grid. An integration is performed over each finite-volume cell:

$$\iiint_V \frac{\partial \hat{\boldsymbol{U}}}{\partial t}\,dV+\iiint_V\left(\frac{\partial \hat{\boldsymbol{F}}}{\partial \xi}+\frac{\partial \hat{\boldsymbol{G}}}{\partial \eta}+\frac{\partial \hat{\boldsymbol{H}}}{\partial \zeta}\right)dV=-\iiint_V \hat{\boldsymbol{J}}\,dV \tag{5}$$

The divergence theorem is then applied to the second integral:

$$\iiint_V \frac{\partial \hat{\boldsymbol{U}}}{\partial t}\,dV+\oiint_S\left(\hat{\boldsymbol{F}}+\hat{\boldsymbol{G}}+\hat{\boldsymbol{H}}\right)\cdot \mathbf{n}\,dS=-\iiint_V \hat{\boldsymbol{J}}\,dV \tag{6}$$

where $\mathbf{n}$: Unit vector normal to the surface (ξ, η, and ζ for $\hat{\boldsymbol{F}}$, $\hat{\boldsymbol{G}}$, and $\hat{\boldsymbol{H}}$, respectively)

S: Closed surface bounding the finite volume (m^2)

Equation (6) is the expression for a generic FVTD formulation. The unknown components of the $\hat{\boldsymbol{U}}$ vector are the magnetic and electric flux densities. The vectors $\hat{\boldsymbol{F}}$, $\hat{\boldsymbol{G}}$, and $\hat{\boldsymbol{H}}$ are the flux vectors and can be expressed in terms of the magnetic and flux densities. A multitude of techniques are used to solve Equation (6) giving rise to the myriad of FVTD numerical algorithms.

E. Flux Evaluation and Time Integration

The flux vectors in Equation (6) can be evaluated numerically using one of several techniques. The technique implemented by Shang is an explicit characteristic-based scheme that produces third-order accuracy. The van Leer's kappa

scheme calculates the flux on a surface of a cell by extrapolating data from adjacent cell centers [10]. The scheme is referred to as a Monotone Upstream-Centered Scheme for Conservation Laws (MUSCL) and is a windward approach that considers the direction of wave propagation. A flux-vector splitting algorithm developed by Steger and Warming [21] is used to calculate the fluxes from the independent variable $\hat{U}$ calculated at the cell faces. The incoming and outgoing electromagnetic waves are split based on the positive and negative sign of the eigenvalue, hence, the name split-flux vectors.

Equation (6), in the temporal or time-stepping domain, can be solved using several techniques, just as in the spatial domain. Shang uses a Runge-Kutta family of single-step multi-stage procedures [13] which gives varying degrees of accuracy. For example, with van Leer's kappa scheme for the flux evaluation, Shang uses a four-stage Runge-Kutta method that produces fourth-order accuracy [10].

F. Boundary Conditions

Shang uses a first-order accurate radiation boundary condition [7-16] in which the incoming flux component is set to zero at the boundary. For the compatibility condition, the fields traveling perpendicular to the boundary are not reflected. For example, in the case of the propagation of a wave from a dipole, the BC is exact since the wave travels along the radial coordinate direction. However, numerical errors can result if the wave is not traveling perpendicular to the boundary. The coordinate transformation discussed previously increases the component of the wave traveling perpendicular to the outer boundary [12].

A surface boundary condition is implemented on the surface of PEC scatterers. The boundary condition sets the tangential electric field equal to zero and the normal component of the magnetic flux density equal to zero [2-3,8].

G. Green's-Function-Based Near-to-Far Field Transformation

The spatial and time integration of Equation (6) gives time-domain results in the near-field whereas the RCS is a far-field calculation. Green's-function-based transformations allow the scattered fields in the far-field to be easily calculated from the near-field results subsequent to a Fourier transform [22].

The far-field results are obtained by creating a virtual surface around the object. An imaginary surface in the FVTD grid space can serve as a virtual surface. The surface equivalence theorem is applied to the surface to obtain the equivalent time-harmonic electric and magnetic currents and charges. The currents and charges on the virtual surface are then weighted by a free-space Green's function to obtain the far-field $\boldsymbol{E}$ and $\boldsymbol{H}$ fields [22]. The far-field is easily calculated from the far-field scattered $\boldsymbol{E}$ and $\boldsymbol{H}$ fields.

II. Electromagnetic Scattering Results

The RCS using the fourth-order accurate characteristic-based FVTD algorithm, implemented by Shang [7-16], for the ogive and cone-sphere test bodies are discussed [24]. Bistatic and monostatic RCS are presented for each perfect electric conducting (PEC) test body and compared to MoM and empirical data to evaluate the FVTD algorithm and code for CEM.

To analyze the scattering from the ogive, a grid convergent study was performed to obtain the optimum grid point density (GPD) for each coordinate direction (r,θ,ϕ). The radial direction is approximately orthogonal to the surface and the theta and phi directions correspond to the surface of the object. The grid for the cone-sphere was generated using the optimal GPDs. The RCS results for the cone-sphere confirm the grid requirements obtained for the ogive and validate the FVTD algorithm for another PEC test body.

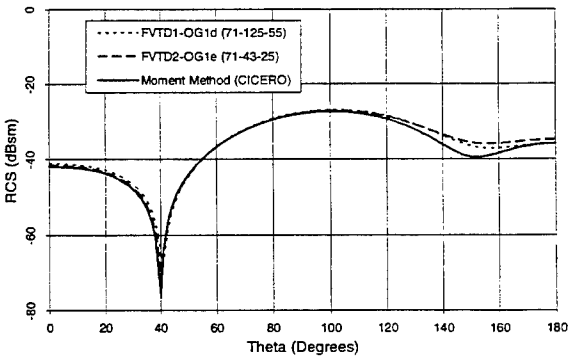

Figure 1: Ogive Bistatic RCS, 1.18 GHz, HH, Fine (71-125-55) vs. Coarse (71-43-25) Grid

A. Ogive Electromagnetic Scattering Results

Three ogive tests, including several subtests, are labeled with a character

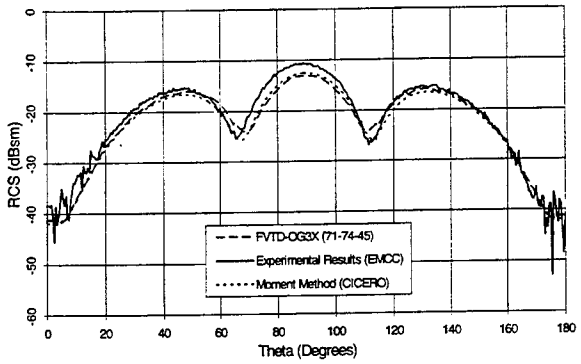

Figure 2: Ogive Monostatic RCS, 1.18 GHz, HH

designator. "OG" in the test designator refers to a test for the ogive, and the number in the test designator refers to the test number. The last letter in each test designator refers to the subtest. The subtests are groups of tests that use a specific frequency or grid size. A designator such as OG3X refers to the entire group of subtests.

The RCS for the ogive for each test are compared to MoM RCS results and experimental data for either VV (transmit vertical, receive vertical) or HH (transmit horizontal, receive horizontal) polarization. The first ogive tests, OG1X, use a sinusoid incident wave at 1.18 GHz. Tests OG3X are monostatic calculations at 1.18 GHz. The bistatic RCS for the ogive at 9.0 GHz is test OG4a. For all of the bistatic tests, the angle of incidence is tip-on at 0°.

The bistatic RCS is calculated for the ogive at 1.18 GHz using a sinusoid incident wave. The ogive is one wavelength long at this frequency. The HH polarization RCS is shown in Figure 1 and compares the RCS for the coarse grid (OG1e) to the fine grid (OG1d). The fine grid has a surface grid point density of 80-116 cells/λ and the coarse grid has a grid point density of 22-32 cells/λ. The FVTD results are within 3.0 dB of the MoM data for the coarse grid and for the fine grid are within 2.0 dB of the MoM.

The frequency data for tests OG1d and OG1e were taken from the fourth to the fifth periods. These tests reveal that for 1.18 GHz the transients introduced with the sinusoid incident wave require at least four periods to diminish before frequency data can be taken for the RCS calculations. Taflove [22] recommends that at least four times the electrical length (in periods) is required. The ogive results show that this approximation is appropriate for this frequency; however, fewer periods are used for higher frequencies to obtain accurate data.

In addition to bistatic RCS, the FVTD code can also obtain monostatic data. Multiple simulations must be completed to obtain monostatic data for one frequency as compared to one test for bistatic data. One simulation produces a bistatic plot for 0° to 180°. The simulation produces a monostatic result for only the angle of incidence. To obtain a full monostatic sweep, a bistatic-to-monostatic approximation is used. The approximation requires tests to be completed every 10° and bistatic data completes the monostatic approximation [6]. Tests OG3X are monostatic calculations for the ogive at 1.18 GHz. A test was completed for an angle of incidence every 10° from 0° to 90°. The ogive is symmetric about the xy plane resulting in a symmetric monostatic plot about θ=90°.

The monostatic approximation for HH polarization is plotted in Figure 2. The HH monostatic test used a moderate grid size of (71-74-45) and frequency data was taken from the fifth to the seventh period. The FVTD RCS is plotted against MoM results and empirical data. As can be seen in the plot, the MoM and FVTD results are almost identical and differ from the empirical data by nearly the same value. FVTD results differ from the MoM by no more than 2.5 dB. If the large fluctuations are ignored in the empirical data, the FVTD results are within 3.1 dB of the empirical data.

Further analysis is completed for the ogive using FVTD by running a test, OG4a, for the ogive at 9.0 GHz. The ogive is approximately 7.6 wavelengths long at this frequency. The grid size

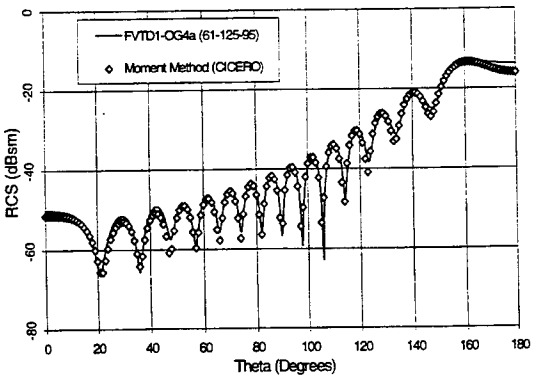

Figure 3: Ogive Bistatic RCS, 9.0 GHz, VV

required for this frequency is much larger (61-125-95). The FVTD results for 9.0 GHz, VV, are shown in Figure 3. The FVTD results are plotted against MoM RCS data. The results are excellent except there are small discrepancies in the backscatter and forward scattering regions. The surface grid point densities (GPD) for these tests are smaller than for 1.18 GHz. The grid point densities in the theta and phi directions are 15.2 cells/λ and 18.8 cells/λ, respectively. The results for the ogive at 1.18 GHz showed that a GPD of at least 22-32 cells/λ gives the best data. These results depict the dependence of the required GPD on the electrical size of the object. The GPD can be 15-20 cells/λ if the electrical length of the object increases.

The 9.0 GHz results for the ogive illustrate the dependence of the length of simulation time (in periods) to the length of the object. At 1.18 GHz, the test had to be at least four times (in periods) the length of the object. The same factor would require a simulation time of 30 periods for 9.0 GHz. This is not required because, at 9.0 GHz, the ogive is in the optical region. At 9.0 GHz, the diffraction and the traveling waves can be considered to be more of a local phenomena than for 1.18 GHz. This reduces the simulation time for the test to approximately three times the length of the object (in periods) instead of four.

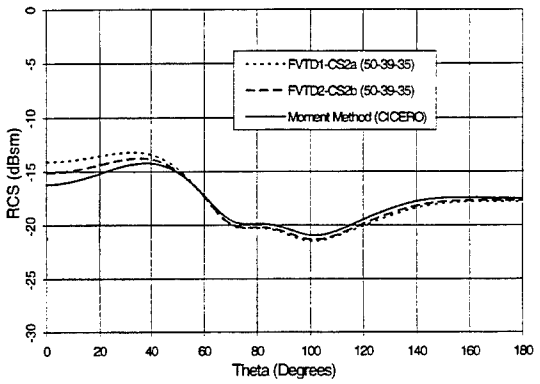

Figure 4: Cone-Sphere Bistatic RCS, 0.869 GHz, VV, Tip-On Incidence

B. Cone-Sphere Electromagnetic Scattering Results

The RCS calculations for the cone-sphere provide further validation of the FVTD code and algorithm. The cone-sphere is a common RCS test body but the narrow cone portion and the sphere cap provide a unique body for analysis. At lower frequencies, the scattering from the cone-sphere can be modeled as traveling waves along the narrow cone, creeping waves around the sphere cap, and diffraction from the tip. Three tests were completed which include several subtests with designators "CS" instead of "OG" to refer to the cone-sphere.

The electromagnetic scattering via FVTD are compared to MoM RCS results and experimental data for VV and HH polarization. The cone-sphere is two wavelengths long at 0.869 GHz. An incident angle of 0° corresponds to incidence on the cone-sphere along the axis of symmetry directly onto the sphere-cap. Tests CS2X are bistatic tests at 0.869 GHz with a sinusoid incident wave at 180° (tip-on incidence). Tests CS3X are tests for the monostatic calculations at 0.869 GHz. The monostatic RCS is computed every 10° from 0° to 180°, and bistatic data completes the monostatic plot. CS5a is a bistatic simulation for the cone-sphere at 3.0 GHz using a sinusoid incident wave at tip-on incidence (θ=180).

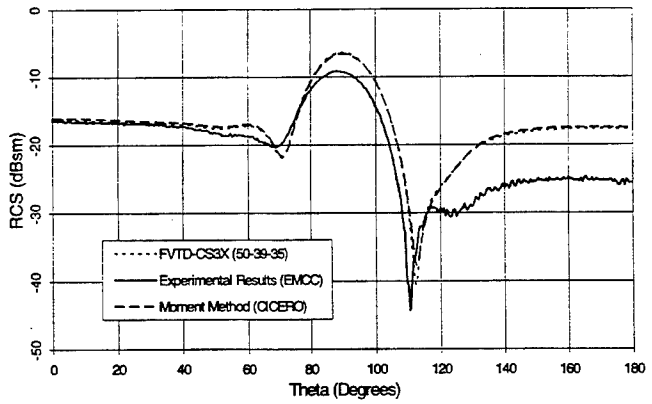

Figure 5: Cone-Sphere Monostatic RCS, 0.869 GHz, HH

FVTD RCS data for tip-on incidence were obtained in test OG2X. The incident wave propagates toward the cone-sphere from 180°. The accuracy of the bistatic RCS depends on the correct calculation of creeping waves, traveling waves, and tip diffraction. The VV polarization case is shown in Figure 4. The finer grid, CS2b,

produces much better results than the grid with the coarser spacing (CS2a) in the radial direction. The forward scatter results (θ=0°) are only accurate if the fine grid is used (CS2b).

The monostatic RCS data for the cone-sphere, HH polarization, is plotted in Figure 5. The FVTD and MoM RCS match each other much closer than they match the empirical data. Volakis [24] states that errors exist in the experimental data, especially in the forward sector (120°-180°). The MoM and FVTD results are almost identical for every location except for several of the bistatic-to-monostatic approximation junctions. The agreement between the techniques suggest that the empirical data is not correct from 120°-180°.

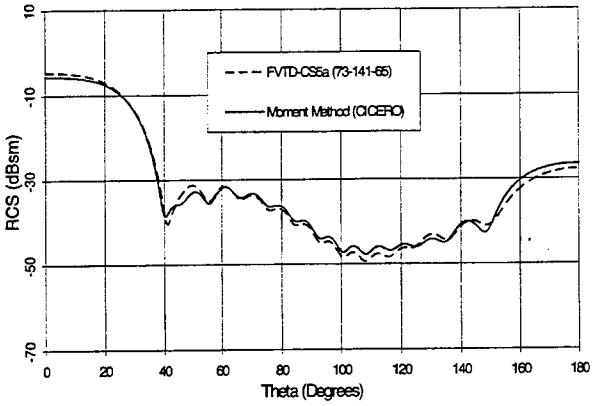

Figure 6: Cone-Sphere Bistatic RCS, 3.0 GHz, VV, Tip-On Incidence

The bistatic RCS for the cone-sphere at 3.0 GHz is presented. Test CS5a is the tip-on incidence test. The length of the cone-sphere is 6.9 wavelengths at this specific frequency. The cone-sphere at this frequency is in the optical region, just as the ogive was for 9.0 GHz. The electromagnetic phenomena, such as diffraction, creeping waves, and traveling waves, are local and the test time (in periods) is not as long as for lower frequencies.

Figure 6 is the VV polarization RCS for tip-on incidence (CS5a). The FVTD results are almost identical to the MoM RCS results. The FVTD RCS data for the forward scatter region, from the sphere-cap (θ=0°), differs by 1.0 dB from the MoM data. The FVTD data for the backscatter region (θ=180°) from the tip differs by 1.2 dB from the MoM RCS results. As seen with the ogive, errors in the FVTD RCS calculations first occur at the tips.

III. Conclusions

The electromagnetic scattering and RCS results for the ogive and cone-sphere test bodies were presented. Bistatic and monostatic RCS results were compared to MoM and empirical RCS results.

The FVTD RCS for the ogive is excellent compared to MoM and empirical data. Several bistatic and monostatic tests at various frequencies showed that a grid point density (GPD) on the surface of approximately 22-32 cells/λ produced the best results for lower frequencies (1.18 GHz) and could be reduced to 15.2-18.8 cells/λ for larger frequencies (9.0 GHz). Shankar [17] reports a GPD requirement of 30-50 cells/λ for objects with edges or tips, like the ogive, for his second-order accurate algorithm. The lower GPD requirement for Shang's fourth-order accurate FVTD code is consistent with the order of accuracy of the algorithms. As the GPD decreases, the errors in the RCS occur first in the backscatter and forward scatter direction as would be expected because of the diffraction at the tips of the ogive. As the electrical size of the object increases, traveling waves and diffraction contribute less to the RCS. These phenomena become local and the grid point density does not have to be as large to accurately compute the propagation of the wave. The bistatic tests for 1.18 GHz differed from the MoM results by no more than 3.0 dB. The FVTD calculations for the monostatic tests were compared to empirical results in addition to MoM results. The FVTD results are within 2.5 dB of the MoM monostatic values and within 3.1 dB of the empirical results.

The bistatic and monostatic cone-sphere results confirm the accuracy and grid requirements for the ogive. For 0.869 GHz, the surface grid spacing required is 22-26 cells/λ. The results differed by no more than 1.6 dB from the MoM results and 0.5 dB from the empirical results. The bistatic RCS for 3.0 GHz differed by no more than 2.1 dB from the MoM results. Accurate results required a surface grid spacing of 14-26 cells/λ to accurately consider diffraction and traveling waves. These grid point density requirements confirm the ogive conclusion that a lower grid point density is needed for electrically larger objects since diffraction and traveling waves contribute less to the RCS.

The electromagnetic phenomena which occurs from the surfaces of an ogive and cone-sphere are challenging for many computational codes. The smooth curved surfaces, tips, and diffraction points are surface characteristics which can pose difficulties for accurately computing scattering results. Based on the FVTD results for the ogive and cone-sphere, the

electrical size of the object is critical when determining grid size and spacing. For a small object, 1-2λ, the grid spacing must be 22-25 cells/λ on the surface. For an object which is electrically larger (7λ-8λ), the surface grid spacing may be reduced to 15-19 cells. These findings are critical for the expansion of the code to studying electrically larger objects such as airfoils and aircraft shaped bodies. A grid must be generated which will incorporate these features for a particular frequency.

Acknowledgments

In support of this work, the authors wish to thank Dr. William Baker, Major Tom Buter, and Major Gerald Gerace of the Air Force Institute of Technology. The authors also wish to thank the assistance of Dr. J.S. Shang and Dr. Kueichien Hill from Wright Laboratory. In addition, this research was supported in part by a grant of HPC time from the DoD HPC Centers, CEWES (Cray 90) and Maui (SP-2).

Bibliography

1. Constantine A. Balanis, *Advanced Engineering Electromagnetics*. New York: John Wiley & Sons, 1989.

2. D.C. Blake and T.A. Buter, "Domain Decomposition Strategies for Solving Hyperbolic Systems on Distributed Parallel Architectures," *AIAA Paper 96-0834*. 34th Aerospace Sciences Meeting and Exhibit, Reno NV, Jan. 1996.

3. D.C. Blake and T.A. Buter, "Overset Grid Methods Applied to a Finite-Volume Time-Domain Maxwell Equation Solver," *AIAA Paper 96-0834*. 27th Fluid Dynamics, Plasmadynamics and Lasers Conference, New Orleans LA, June 1996.

4. J.W. Crispin, Jr. and K.M. Siegel, *Methods of Radar Cross Section Analysis*. New York: Academic Press, 1968.

5. Karl S. Kunz and Raymond J. Luebbers, *The Finite Difference Time Domain Method for Electromagnetics*. Boca Raton: CRC Press, 1993.

6. Michael J. Schuh, Alex C. Woo, and Michael P. Simon, "The Monostatic/Bistatic Approximation," *IEEE Antennas and Propagation Magazine*, vol. 36, no. 4, pp. 76-78, Aug. 1994.

7. J.S. Shang, "A Characteristic-Based Algorithm for Solving 3-D, Time-Domain Maxwell Equations," *AIAA Paper 92-0452*. 30th Aerospace Sciences Meeting and Exhibit, Reno NV, Jan. 1992.

8. J.S. Shang, "Characteristic-Based Algorithms for Solving Maxwell's Equations in the Time-Domain," *IEEE Antennas and Propagation Magazine*, vol. 37, no. 3, pp. 15-25, June 1995.

9. J.S. Shang, "A Fractional-Step Method for Solving 3-D Time-Domain Maxwell Equations," *Journal of Computational Physics*, vol. 118, pp. 109-119, 1995.

10. J.S. Shang and Robert M. Fithen, "A Comparative Study of Numerical Algorithms for Computational Electromagnetics," *AIAA Paper 94-2410*. 25th AIAA Plasmadynamics and Lasers Conference, Colorado Springs CO, June 1994.

11. J.S. Shang, D.A. Calahan, and B. Vikstrom, "Performance of a Finite Volume CEM Code on Multicomputers," *AIAA Paper 94-0236*. 32nd Aerospace Sciences Meeting and Exhibit, Reno NV, Jan. 1994.

12. J.S. Shang and D. Gaitonde, "Characteristic-Based Time-Dependent Maxwell Equations Solvers on a General Curvilinear Frame," *AIAA Paper 93-3178*. 24th AIAA Plasmadynamics and Laser Conference, Orlando FL, July 1993.

13. J.S. Shang and D. Gaitonde, "On High Resolution Schemes for Time-Dependent Maxwell Equations," *AIAA Paper 96-0832*. 34th Aerospace Sciences Meeting and Exhibit, Reno NV, Jan. 1996.

14. J.S. Shang and D. Gaitonde, "Scattered Electromagnetic Field of a Reentry Vehicle," *AIAA Paper 94-0231*. 32nd Aerospace Sciences Meeting and Exhibit, Reno NV, Jan. 1996.

15. J.S. Shang and S.J. Scherr, "Time-Domain Electromagnetic Scattering Simulations on Multicomputers," *AIAA Paper 95-1966*. 26th AIAA Plasmadynamics and Lasers Conference, San Diego CA, June 1995.

16. J.S. Shang and C.C. Shang, "Concurrent Computation of Electromagnetic Phenomena on the Paragon," *AIAA Paper 95-0592*. 33rd Aerospace Sciences Meeting and Exhibit, Reno NV, Jan. 1995.

17. Vijaya Shankar, "Computational Electromagnetics (CEM) - Development of a Finite-Volume, Time-Domain Solver for Maxwell's Equations," Report NAWCADWAR-93052-60, Contract N62269-90-C-0257, Thousand Oaks, CA: Rockwell International Science Center, 1993.

18. Vijaya Shankar, "Research to Application - Supercomputing Trends for the 90's, Opportunities for Interdisciplinary Computations," *AIAA Paper 91-0002*. 29th Aerospace Sciences Meeting, Reno NV, Jan. 1991.

19. Vijaya Shankar, W.F. Hall, and A.H. Mohammadian, "A CFD-based Finite-Volume Procedure for Computational Electromagnetics - Interdisciplinary Applications of CFD Methods," *AIAA Paper 89-1987*. 9th AIAA Computational Fluid Dynamics Conference, Buffalo NY, June 1989.

20. Vijaya Shankar, W.F. Hall, and A.H. Mohammadian, "A Time-Domain, Finite-Volume Treatment for the Maxwell Equations," *Electromagnetics*, vol. 10, pp. 127-145, 1990.

21. Joseph L. Steger and R.F. Warming, "Flux Vector Splitting of the Inviscid Gasdynamic Equations with Application to Finite-Difference Methods," *Journal of Computational Physics*, vol. 40, pp. 263-293, 1981.

22. Allen Taflove, *Computational Electrodynamics: The Finite-Difference Time-Domain Method*. Boston: Artech House, 1995.

23. Bram van Leer, "Flux-Vector Splitting For the Euler Equations," Eighth International Conference on Numerical Methods in Fluid Dynamics, Berlin: Springer-Verlag, pp. 507-512, 1982.

24. John L. Volakis, Alex C. Woo, Helen T.G. Wang, Michael J. Schuh, and Michael L. Sanders, "Benchmark Radar Targets for the Validation of Computational Electromagnetics Programs," *IEEE Antennas and Propagation Magazine*, vol. 35, no. 1, pp. 84-89, Feb. 1993.